

Magnetic gradient free two axis control of a valley spin qubit in SiGe

Y.-Y. Liu,¹ L. A. Orona,¹ Samuel F. Neyens,² E. R. MacQuarrie,² M. A. Eriksson,² and A. Yacoby¹

¹*Department of Physics, Harvard University, Cambridge, Massachusetts 02138, USA*

²*University of Wisconsin-Madison, Madison, 53706, Wisconsin, USA*

(Dated: January 26, 2021)

Spins in SiGe quantum dots are promising candidates for quantum bits but are also challenging due to the valley degeneracy which could potentially cause spin decoherence and weak spin-orbital coupling. In this work we demonstrate that valley states can serve as an asset that enables two-axis control of a singlet-triplet qubit formed in a double quantum dot without the application of a magnetic field gradient. We measure the valley spectrum in each dot using magnetic field spectroscopy of Zeeman split triplet states. The interdot transition between ground states requires an electron to flip between valleys, which in turn provides a g-factor difference Δg between two dots. This Δg serves as an effective magnetic field gradient and allows for qubit rotations with a rate that increases linearly with an external magnetic field. We measured several interdot transitions and found that this valley introduced Δg is universal and electrically tunable. This could potentially simplify scaling up quantum information processing in the SiGe platform by removing the requirement for magnetic field gradients which are difficult to engineer.

INTRO

Quantum algorithms have been proposed to solve problems that are formidable for classical computers [1–4] but require quantum hardware to be implemented. Electron spins confined to gate defined semiconductor quantum dots hold promise as quantum bits (qubits) due to the promise of long coherence times and the localized nature of their control, making them promising for scaling up to the large number of qubits required for real algorithms [5–8]. These qubits have demonstrated fast initialization, high fidelity readout [9, 10], and the possibility of operating at temperatures above 1 Kelvin [11, 12]. Single spin qubits have demonstrated high fidelity single qubit gates of 99.9% [13] and two qubit gates above 98% [14]. While the difficulty in addressing single spin qubits might be an obstacle for scaling up, singlet-triplet qubits have the advantage of having a Hamiltonian whose magnitude and direction can be electrically tuned from the exchange energy axis to an additional control axis generated by a magnetic field gradient, ΔB_Z [15, 16].

Among all semiconductor platforms, silicon/silicon-germanium (Si/SiGe) is appealing because its weak nuclear spin background minimizes the decoherence caused by magnetic field fluctuations [8, 17]. Moreover, weak spin-orbit coupling further reduces the spin relaxation caused by charge fluctuation. This, however, is a double edged sword, because spin-orbital coupling can also be used for electrical spin control. In the absence of full electrical control, other works have used micromagnets placed near the qubit to create a local magnetic field gradient for an effective spin drive [7, 13, 16, 18]. Strong field gradients, however, are hard to create over large areas of the sample, posing challenges for scaling up this scheme. Another challenge to developing a high fidelity spin qubit in Si/SiGe is the valley degeneracy, which may also contribute to spin decoherence [19]. This degeneracy

can be measured using magneto spectroscopy, Hall Bar measurements and microwave readout in hybrid cavity quantum electrodynamic (cQED) systems [20–22] and can be removed by lattice strain and electrostatic confinement [21, 23].

In this work we investigate a valley-assisted spin qubit formed in SiGe double quantum dots which does not require a magnetic field gradient to achieve full two axis single qubit control. For interdot transitions where the electron number is $(4n, 4m) - (4n \pm 1, 4m \mp 1)$, where n and m are integers, valley flipping is required for transitions between ground states in each dot. We use a spin funnel scheme [9] to map the valley spectrum in each dot. The valley splitting can be tuned using gate controlled electric fields [19, 21, 24]. Here we show that valley flipping between the interdot transition provides a g-factor difference and generates a ΔB_Z rotation whose precession rate increases linearly with increasing magnetic field. Importantly, this valley introduced g-factor gradient is also electric field dependent. The combined dependence on the magnetic and electrical fields enables a tunable ΔB_Z rotation. This could potentially simplify scaling up quantum information processing as it removes the need for an external magnetic field gradient.

DEVICE AND METHOD

Figure 1(a) shows a scanning electron microscope image of a typical device that utilizes an overlap gate geometry to achieve quantum dot confinement [25]. The barrier gates, B, create potential barriers for controlling tunneling rates and plunger gates, P, select the charge state in each dot and tune their chemical potential. For this experiment, a double quantum dot (DQD, marked in yellow) is formed at the left two plunger gates P_1 to P_2 , while P_3 to B_5 control the tunneling rate to a fermi

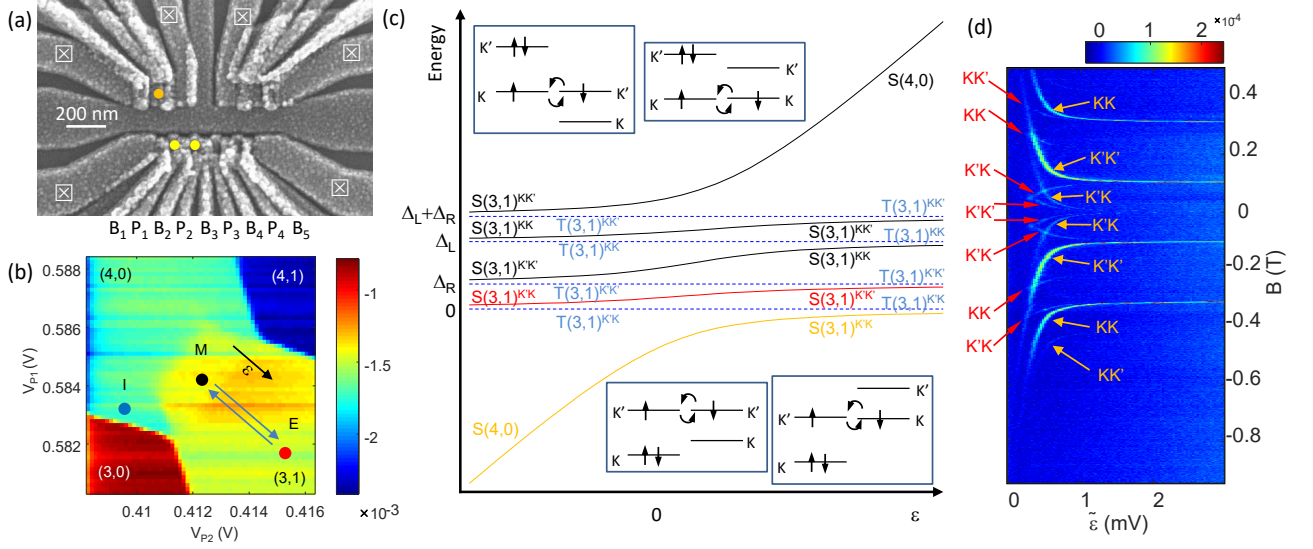


Figure 1. (a) SEM of an overlap style device. The DQD and sensor location are labeled as yellow and orange dots, respectively. (b) Charge stability diagram measured by performing charge readout as a function of plunger gate voltages after being prepared in a random $(3,1)$ state. Spin blockade will keep triplet in configuration $(3,1)$ and singlet in configuration $(4,0)$ in the bright area in the $(4,0)$ region, giving rise to the readout spot M . The spot I is for the initialization of a singlet and spot E is for qubit gate operation. (c) Schematic level diagram as a function of ϵ with the singlet plotted as solid lines and triplets plotted as blue dashed lines. Inset: four possible $(3,1)$ states interact with S_{40} . (d) Spin funnel obtained by measuring the cross over of singlet to triplet states as a function of B and $\tilde{\epsilon}$. Two sets of curvatures are observed, as emphasized by the red and yellow arrows. The valley states of the triplets are labeled accordingly.

sea. We also form a sensor dot (marked in orange) to perform charge detection and use RF-reflectometry for fast readout.

Figure 1(b) demonstrates Pauli-blockade at the $(4,0)$ - $(3,1)$ transition, as required for forming a singlet-triplet qubit. The energy states of the DQD are dependent on which of the two valley eigenstates, K or K' , the electrons occupy. Here we note that valley states K and K' can be different between dots, and thus there is no orthogonality, which allows valley states to flip during interdot transitions. In the $(4,0)$ charge state the four spin valley combinations of the ground orbital state are completely filled. The spin blockade region shown in Fig. 1(b) is cut-off at low ϵ by transitions into the excited orbital state, which is $200 \mu\text{eV}$ higher than the ground state and allows the triplet states to decay into $(4,0)$ states. This energy is large enough to be ignored in the spin dynamics discussed below.

The insets of Fig. 1(c) show the four possible $(3,1)$ states that the ground $(4,0)$ state can transition to without a spin flip. We use the notation $(3,1)^{ij}$ where the superscript i represents the valley of the vacancy in the left dot and j represents the valley of the electron in the right dot. The ground $(3,1)$ charge state is then $(3,1)^{K'K}$ and the transition from $(4,0)$ to $(3,1)^{K'K}$ requires flipping an electron from the K' valley to the K valley, suggesting that there is a valley difference between these two states. Assuming that the valley splitting in the left(right) dot

is $\Delta_{L(R)}$, the three excited $(3,1)$ valley states would be $(3,1)^{K'K'}$, $(3,1)^{KK}$ and $(3,1)^{KK'}$ and are Δ_L , Δ_R and $\Delta_L + \Delta_R$ higher in energy compared to the $(3,1)^{K'K}$ state.

Figure 1(c) plots the energy diagram of all relevant states as a function of detuning ϵ between the chemical potential of ground $(4,0)$ and $(3,1)$ charge states. The interdot coupling t_c opens up the avoided crossing of all $(4,0)$ - $(3,1)$ singlet transitions, and leads to the hybridization of different $S(3,1)^{ij}$ singlets when $2t_c \gtrsim \Delta_{L(R)}$ as shown by the solid lines in Fig. 1(c). For all $(3,1)$ triplet states, the Pauli blockade forbids the interdot transition and give rise to the energy levels as shown by the blue dashed lines. An external magnetic field B_z will further introduce Zeeman splitting $E_Z = \pm g\mu_B B_z$ that lift the degeneracy of triplet states (not shown in the figure).

SPIN FUNNEL

Spin funnel measurements can extract the exchange energy $J(\epsilon)$ between the singlet and zero angular momentum triplet state, T_0 , by detecting the S - T_+ degeneracy as a function of magnetic field B and ϵ [9]. This allows us to map $J(\epsilon)$ to the Zeeman energy $E_Z^c = g\mu_B B_z^c$. In order to detect this degeneracy, we first prepare the DQD in a singlet by loading the ground $(4,0)$ state at the spot I in Fig. 1(b) and then park at spot M . We then abruptly pulse the DQD to the exchange location E and evolve

for a time of $\tau_E = 1 \mu\text{s}$. Finally, we perform readout of the spin state at position M. During the process we keep the pulse along the diagonal (ϵ) direction such that $\Delta V_{P_2} = -\Delta V_{P_1} = \tilde{\epsilon}$ with a lever arm that converts from gate potential to energy given by $\epsilon = 0.25\tilde{\epsilon}$ meV/mV. At a detuning where $E_Z = J(\epsilon)$, an interaction between the singlet state and the degenerate T_+ state results in a finite probability P_T of flipping the state into a triplet state [15, 26]. Fig. 1(d) demonstrates the funnel data over $\tilde{\epsilon} = 0 - 3$ mV and a magnetic field range $B = -0.9 \sim 0.5$ T. A multitude of spin funnel features symmetric in magnetic field are clearly observed indicating multiple triplet branches become degenerate with different singlet states.

The orange arrows point to 4 pairs of spin funnels where $E_z^c(\tilde{\epsilon})$ is quickly changing with $\tilde{\epsilon}$. The 1st pair approaches zero field at large $\tilde{\epsilon}$ and maps out the the ground state singlet energy that is plotted as the orange line in Fig. 1(c). This results from the crossing of this ground singlet state and $T_+(3, 1)^{K'K}$. The other 3 pairs are parallel to the first spin funnel and offset by $12 \mu\text{eV}$, $33 \mu\text{eV}$ and $45 \mu\text{eV}$, which corresponds to the intersection between the ground singlet and $T_+(3, 1)^{K'K'}$, $T_+(3, 1)^{KK}$ and $T_+(3, 1)^{KK'}$. We have also noticed that the 2nd and 3rd pair are brighter, which suggests a larger P_T at these transitions. This is expected because flipping the singlet $S(4, 0)$ to the $T_+(3, 1)^{K'K'}$ or $T_+(3, 1)^{KK}$ states does not require flipping the valley of the transitioning electron (Fig. 1(c) insets) suggesting the valley states maybe similar between dots. From these observations we find valley splittings of $12 \mu\text{eV}$ and $33 \mu\text{eV}$ but we cannot tell which corresponds to Δ_L or Δ_R . We take $\Delta_L > \Delta_R$ for convenience in the following discussion.

Our experiments take place with an electron temperature of around 100 mK, which causes us to load the excited singlet state, $S(3, 1)^{K'K'}$, with approximately a 10% probability. The energy spectrum of this state is plotted as the red curve in Fig. 1(c). We observe signatures of the degeneracy between this excited singlet state and the 4 triplet states as an additional four sets of curvatures indicated by the red arrows in Fig. 1(d). The curvatures near $B = 0$ maps the degeneracy between $S(3, 1)^{K'K'}$ and $T_+(3, 1)^{K'K'}$. The crossing between $S(3, 1)^{K'K'}$ and $T_+(3, 1)^{KK}$ and $T_+(3, 1)^{KK'}$ leads to parallel curves with offsets of $\Delta_R - \Delta_L = 21 \mu\text{eV}$ and $\Delta_L = 33 \mu\text{eV}$ relative to zero field. The crossing between $S(3, 1)^{K'K'}$ and $T_-(3, 1)^{K'K}$ gives rise to curvatures with an offset of $\Delta_R = 12 \mu\text{eV}$ relative to zero field and a flipped direction of curvature in response to the magnetic field because it is from the opposite Zeeman branch.

Figure 2(a) overlaps fits for the ground and first excited singlet energies (red and orange curve in Fig. 1(c)) with the funnel data in Fig. 1(d). The fitting finds reasonable agreement between the model and data using the interdot coupling as the only free parameter with a best fit of $t_c = 15 \mu\text{eV}$. We further utilize this spectroscopy

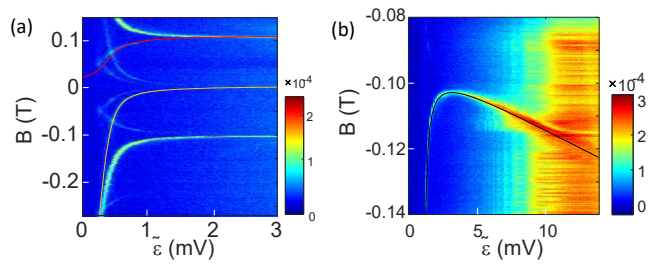


Figure 2. (a) Fit to the first order spin funnel lines in Fig. 1(d). (b) Funnel measurements when the magnetic field zooms in the second branch and $\tilde{\epsilon}$ extend the over large range to explore the gate dependence of the valley splitting.

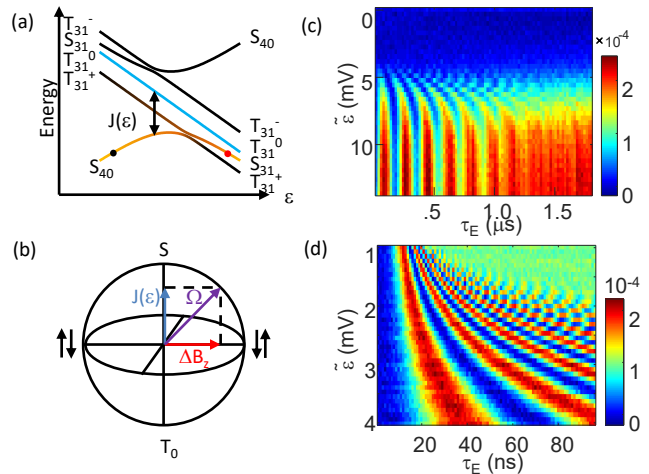


Figure 3. (a) level diagram of relevant states for qubit. The ground singlet (orange) and T^0 (blue) states are the base of the singlet-triplet qubit. (b) The Bloch sphere for singlet-triplet qubit. (c-d) the charge readout as a function of $\tilde{\epsilon}$ and exchange time after the ΔB_Z rotation (c) and the exchange rotation (d).

method to measure the gate dependence of $\Delta_{L(R)}$. Fig. 2(b) shows the second funnel in greater detail by reducing the range of E_z^c and enlarging the range of $\tilde{\epsilon}$. We fit the curve assuming $\Delta_R = \Delta_{R0} + \tilde{\epsilon}\Delta'_R$ and find $\Delta'_R = 0.3$ meV/V. Similarly we find $\Delta'_L = -0.09$ meV/V. [27] Assuming that $\Delta_{L(R)}$ is only dependent on $P_{1(2)}$ we have $\partial\Delta_{L/R}/\partial V_{P_{1(2)}} = 0.3(0.09)$ meV/V, which is comparable to results reported in previous works [19, 21, 23, 24].

TUNABLE TWO AXIS CONTROL

Coherent qubit control is explored in the subspace spanned by $S(4, 0)$ and $(3, 1)^{K'K}$, as demonstrated in Fig. 3(a). The energy gaps between the other $(3, 1)$ valley states and $(3, 1)^{K'K}$ are much larger than the qubit energy scales and can be neglected when considering qubit operations. The ground singlet (orange) and

$T_0(3,1)^{K'K}$ (blue) constitute the basis of the qubit and the Hamiltonian in this subspace can be approximated by $H = J(\epsilon)\sigma_z + (g_L B_{zL} - g_R B_{zR})\mu_B\sigma_x$. Here $\sigma_{x,z}$ are the Pauli operators, $g_{L(R)}$ and $B_{zL(R)}$ are the g-factor and external field at left(right) dot. This system can achieve flexible two axis control, as illustrated by the Bloch sphere in Fig. 3(b) [8, 16]. Rotation along the Z axis can be performed near the interdot transition where $J(\epsilon)$ is large and $\{S, T_0\}$ are the eigenstate of the system Hamiltonian. X axis rotations (ΔB_z rotations) are achieved at large ϵ where $J(\epsilon)$ is negligible and the energy splitting is set by $\mu_B(g_L B_{zL} - g_R B_{zR})$ and the eigenstates are $|\uparrow\downarrow\rangle$ and $|\downarrow\uparrow\rangle$ [15, 16].

We characterize the ΔB_z rotations by initializing the system in $S(4,0)$ and then pulsing the DQD to large ϵ to turn off J , allowing the qubit to rotate around the ΔB_z axis into superpositions of S and T_0 . We then pulse back to M for readout [15, 16]. Figure 3(c) demonstrates charge readout as a function of exchange time τ_E and location ($\tilde{\epsilon}$) when we set the field $B_z = 1$ T. For large $\tilde{\epsilon} > 10$ mV, we find an oscillation at a frequency $f_{\Delta B_z} = \mu_B(g_L B_{zL} - g_R B_{zR})/\hbar = 5.5$ MHz. The decay in the oscillation amplitude indicates a $T_2^* = 1 \mu s$ [27]. When $\tilde{\epsilon} < 10$ mV, the oscillation rate is larger than $f_{\Delta B_z}$ and the amplitude is smaller, indicating a finite $J(\epsilon)$, which contributes to the rotation rate and shifts the angle from the ΔB_z axis. The coherent J rotation can be characterized by a similar process by adding adiabatic ramping before and after the exchange rotation to map S to $|\downarrow\uparrow\rangle$ and T_0 to $|\uparrow\downarrow\rangle$ [9]. The result is presented in Fig. 3(d). For $1 < \tilde{\epsilon} < 4$ mV the rotation amplitude is maximized and the rotation rate is strongly dependent on $\tilde{\epsilon}$. Here J is dominant, and the rotation rate is electrically tunable as expected.

We emphasize that no micromagnet or other external magnetic field gradient source was added to this device. To explore the mechanism responsible for the field gradient, we measure $f_{\Delta B_z}$ as a function of B_z . Figure 4(a) plots charge readout as a function of τ_E and B_z after a ΔB_z rotation at $\tilde{\epsilon} = 10$ mV such that $J(\tilde{\epsilon})$ is negligible. The ΔB_z rotation rate is then extracted and plotted as a function of field in Figure 4(b). This result is consistent with a difference in the g factor of the two dots of around $\Delta g = 3.8 \times 10^{-4} = 0.02\%g$. We note that the two dots' ground states occupy different valley states and this Δg is consistent with the g factor difference between valleys as previously reported [28, 29].

This valley introduced Δg allows the rate of the ΔB_z rotations to be tuned by an external magnetic field. We expect the ΔB_z rotation rate would be 14 MHz at 3 T (beyond the current limit of our magnet), comparable to the field gradient generated by a micro-magnet [16]. This would potentially reduce design complexity for a large array of spin qubits because it eliminates the need for an artificially generated field gradient.

In order to verify the generality of this phenomena,

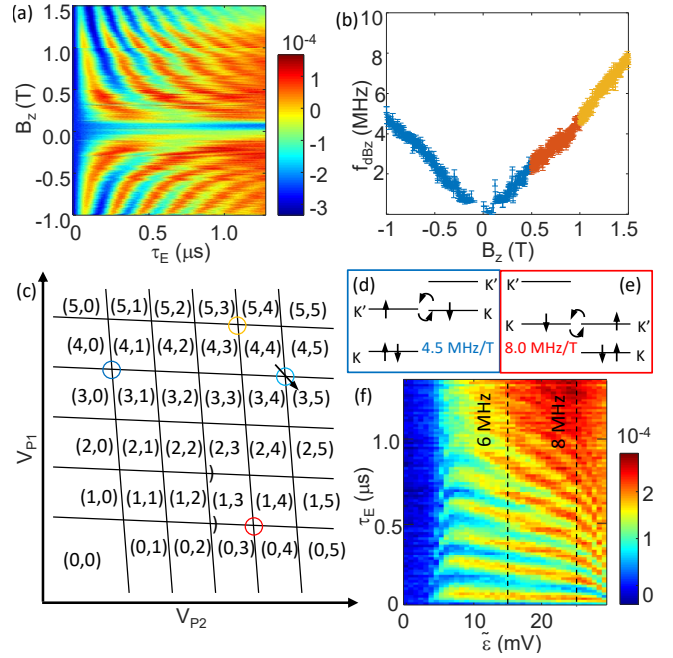


Figure 4. (a) The charge readout as a function of exchange time and magnetic field after a ΔB_z rotation with $\tilde{\epsilon} = 10$ mV (b) After ΔB_z rotation rate as a function of magnetic field. (c) Schematic of a charge stability diagram. Colored circles labels the transitions that satisfy $(4n, 4m)-(4n\pm 1, 4m\mp 1)$. The arrow indicates the direction of ϵ . (d-e) The ground state transition at (d) (4,0)-(3,1) and (e) (0,4)-(1,3) charge configuration and the associated $f_{\Delta B_z}/B_z$ (f) The charge readout as a function of $\tilde{\epsilon}$ and exchange time after the δB_z rotation at (4,4) transition. Dashed lines indicates the range of $\tilde{\epsilon}$ that X axis rotation is dominant and the rotation rate is labeled on top. The gradient of ΔB_z rotation is 2MHz/10mV.

we measured other $(4n, 4m)-(4n\pm 1, 4m\mp 1)$ transitions where the 4 valley spin states are all filled up in one dot and the relevant orbital of the other dot is empty. As previously described, near these transitions the ground states of the $(4n, 4m)$ and $(4n\pm 1, 4m\mp 1)$ states occupy different valley states, which introduce a Δg to the singlet-triplet qubit Hamiltonian.

Figure 4(c) labels these $(4n, 4m)-(4n\pm 1, 4m\mp 1)$ transitions with colored circles in the charge stability diagram. Fig. 4(d) demonstrates the ground states for the (4,0)-(3,1) transition, which is the symmetric configuration compared to the (0,4)-(1,3) transition as demonstrated in Fig. 4(e). At the (1,3)-(0,4) transition, we measure $f_{\Delta B_z}/B_z = 8$ MHz/T which is almost double the value for the (4,0)-(3,1) transition. V_{P1} and V_{P2} have been changed by 100 mV, which allows us to estimate that the gradient can be tuned at a rate of 35 MHz/(T · V). The (4,4)-(3,5) transition has the same filling as Fig. 4(d) and (5,3)-(4,4) transition corresponds to Fig. 4(e). Although the two transitions are close in the charge stability diagram, we find a dramatic change in the Δg . At the (5,3)-(4,4) we find $f_{\Delta B_z}/B_z = 0$ and at the (4,4)-(3,5)

transition $f_{\Delta B_z}/B_z = 5.5$ MHz/T at $\tilde{\epsilon} = 15$ mV.

This drastic change indicates a strong gate dependence of Δg . Figure 4(f) demonstrates the ΔB_z rotation at the (4,4)-(3,5) transition using charge readout as a function of $\tilde{\epsilon}$ and τ_E . Unlike the (4,0)-(3,1) transition where the oscillation rate is a constant once $\tilde{\epsilon} > 10$ mV, we find this frequency increases with $\tilde{\epsilon}$ once $\tilde{\epsilon} > 8$ mV at the (4,4)-(3,5) transition. The oscillation amplitude is maximized in this regime, indicating that J is always negligible such that the rotation is along X axis with the rate only determined by $f_{\Delta B_z}$. At $\tilde{\epsilon} = 15$ mV $f_{\Delta B_z}/B_z = 6$ MHz/T and at $\tilde{\epsilon} = 25$ mV, $f_{\Delta B_z}/B_z$ has increased by 2MHz/T. If we linearly interpolate $f_{\Delta B_z}/B_z$ for $\tilde{\epsilon} < 10$ mV, we expect the $f_{\Delta B_z}/B_z = 0$ at $\tilde{\epsilon}_0 = -15$ mV. The (5,3)-(4,4) transition is located at $\Delta V_{P1} = -\Delta V_{P2} > 40$ mV from the (4,4)-(3,5) transition and thus $\tilde{\epsilon} < \tilde{\epsilon}_0$. Hence $f_{\Delta B_z}/B_z = 0$ at the (5,3)-(4,4) transition is not completely surprising due to this rapid change in Δg at the (4,4)-(3,5) transition.

The g factor difference between valleys has been explained by spin-orbital coupling in previous works [28, 29]. A gate dependent g factor has been predicted for SiGe [29] and observed in Si-MOS system [30]. The gate dependence of the g factor observed here could enable gate operations that require fast changes in ΔB_z . Compared to the field gradient generated by a micro-magnet, $f_{\Delta B_z}$ by Δg can be arbitrarily high with increasing external field. As with the valley splitting, a maximized Δg is expected for an atomically flat Si/SiGe interface and high external electrical field. We thus expect a potentially higher ΔB_z gate fidelity with better substrates and smaller QDs.

CONCLUSION

In this work we have investigated DQD transitions where the electron number is $(4n, 4m)-(4n \pm 1, 4m \mp 1)$. The funnel measurements there provide the valley spectrum in each dot. The extracted valley splitting demonstrates a gate dependence, as observed in previous works. The ground state in each dot occupies a different valley state which provides a g-factor difference between the two charge states. This g-factor gradient generates a ΔB_z rotation that is linear to an external magnetic field and is also gate dependent. These two dependencies provide a tunable ΔB_z rotation that does not require a micro-magnet. This would potentially simplify scaling up to large arrays of spin qubits for quantum information processing.

ACKNOWLEDGEMENT

We acknowledge Lisa Edge from HRL Laboratories for the growth and distribution of the Si/SiGe heteros-

tuctures that were used in this experiment. This work was sponsored by the Army Research Office (ARO), and was accomplished under Grant Number W911NF-17-1-0274 and W911NF-17-1-0202. We acknowledge the use of facilities supported by NSF through the UW-Madison MRSEC (DMR-1720415) and the MRI program (DMR-1625348). The views and conclusions contained in this document are those of the authors and should not be interpreted as representing the official policies, either expressed or implied, of the Army Research Office (ARO), or the U.S. Government. The U.S. Government is authorized to reproduce and distribute reprints for Government purposes notwithstanding any copyright notation herein.

-
- [1] R. D. Somma, S. Boixo, H. Barnum, and E. Knill, Quantum simulations of classical annealing processes, *Physical review letters* **101**, 130504 (2008).
 - [2] G. Carleo and M. Troyer, Solving the quantum many-body problem with artificial neural networks, *Science* **355**, 602 (2017).
 - [3] A. Aspuru-Guzik, A. D. Dutoi, P. J. Love, and M. Head-Gordon, Simulated quantum computation of molecular energies, *Science* **309**, 1704 (2005).
 - [4] P. W. Shor, Polynomial-time algorithms for prime factorization and discrete logarithms on a quantum computer, *SIAM review* **41**, 303 (1999).
 - [5] V. N. Golovach, M. Borhani, and D. Loss, Electric-dipole-induced spin resonance in quantum dots, *Phys. Rev. B* **74**, 165319 (2006).
 - [6] J. J. Morton and B. W. Lovett, Hybrid Solid-State Qubits: The Powerful Role of Electron Spins, *Annual Review of Condensed Matter Physics* **2**, 189 (2011).
 - [7] L. Vandersypen, H. Bluhm, J. Clarke, A. Dzurak, R. Ishihara, A. Morello, D. Reilly, L. Schreiber, and M. Veldhorst, Interfacing spin qubits in quantum dots and donors—hot, dense, and coherent, *npj Quantum Information* **3**, 1 (2017).
 - [8] B. M. Maune, M. G. Borselli, B. Huang, T. D. Ladd, P. W. Deelman, K. S. Holabird, A. A. Kiselev, I. Alvarado-Rodriguez, R. S. Ross, A. E. Schmitz, et al., Coherent singlet-triplet oscillations in a silicon-based double quantum dot, *Nature* **481**, 344 (2012).
 - [9] J. R. Petta, A. C. Johnson, C. M. Marcus, M. P. Hanson, and A. C. Gossard, Manipulation of a Single Charge in a Double Quantum Dot, *Phys. Rev. Lett.* **93**, 186802 (2004).
 - [10] C. B. Simmons, J. R. Prance, B. J. Van Bael, T. S. Koh, Z. Shi, D. E. Savage, M. G. Lagally, R. Joynt, M. Friesen, S. N. Coppersmith, et al., Tunable Spin Loading and T_1 of a Silicon Spin Qubit Measured by Single-Shot Readout, *Phys. Rev. Lett.* **106**, 156804 (2011).
 - [11] L. Petit, H. G. J. Eenink, M. Russ, W. I. L. Lawrie, N. W. Hendrickx, S. G. J. Philips, J. S. Clarke, L. M. K. Vandersypen, and M. Veldhorst, Universal quantum logic in hot silicon qubits, *Nature* **580**, 355 (2020).
 - [12] C. H. Yang, R. C. C. Leon, J. C. C. Hwang, A. Saraiva, T. Tanttu, W. Huang, J. Camirand Lemyre, K. W. Chan,

- K. Y. Tan, F. E. Hudson, et al., Operation of a silicon quantum processor unit cell above one kelvin, *Nature* **580**, 350 (2020).
- [13] K. Takeda, J. Yoneda, T. Otsuka, T. Nakajima, M. R. Delbecq, G. Allison, Y. Hoshi, N. Usami, K. M. Itoh, S. Oda, et al., Optimized electrical control of a Si/SiGe spin qubit in the presence of an induced frequency shift, *npj Quantum Information* **4**, 54 (2018).
- [14] W. Huang, C. H. Yang, K. W. Chan, T. Tanttu, B. Hensen, R. C. C. Leon, M. A. Fogarty, J. C. C. Hwang, F. E. Hudson, K. M. Itoh, et al., Fidelity benchmarks for two-qubit gates in silicon, *Nature* **569**, 532 (2019).
- [15] S. Foletti, H. Bluhm, D. Mahalu, V. Umansky, and A. Yacoby, Universal quantum control of two-electron spin quantum bits using dynamic nuclear polarization, *Nature Physics* **5**, 903 (2009).
- [16] X. Wu, D. R. Ward, J. R. Prance, D. Kim, J. K. Gamble, R. T. Mohr, Z. Shi, D. E. Savage, M. G. Lagally, M. Friesen, et al., Two-axis control of a singlet-triplet qubit with an integrated micromagnet, *Proc Natl Acad Sci USA* **111**, 11938 (2014).
- [17] R. Hanson, L. P. Kouwenhoven, J. R. Petta, S. Tarucha, and L. M. Vandersypen, Spins in few-electron quantum dots, *Reviews of modern physics* **79**, 1217 (2007).
- [18] D. M. Zajac, A. J. Sigillito, M. Russ, F. Borjans, J. M. Taylor, G. Burkard, and J. R. Petta, Resonantly driven CNOT gate for electron spins, *Science* **359**, 439 (2018).
- [19] C. H. Yang, A. Rossi, R. Ruskov, N. S. Lai, F. A. Mohiyaddin, S. Lee, C. Tahan, G. Klimeck, A. Morello, and A. S. Dzurak, Spin-valley lifetimes in a silicon quantum dot with tunable valley splitting, *Nature Communications* **4**, 2069 (2013).
- [20] M. G. Borselli, R. S. Ross, A. A. Kiselev, E. T. Croke, K. S. Holabird, P. W. Deelman, L. D. Warren, I. Alvarado-Rodriguez, I. Milosavljevic, F. C. Ku, et al., Measurement of valley splitting in high-symmetry Si/SiGe quantum dots, *Appl. Phys. Lett.* **98**, 123118 (2011).
- [21] S. Goswami, K. A. Slinker, M. Friesen, L. M. McGuire, J. L. Truitt, C. Tahan, L. J. Klein, J. O. Chu, P. M. Mooney, D. W. van der Weide, et al., Controllable valley splitting in silicon quantum devices, *Nature Physics* **3**, 41 (2007).
- [22] X. Mi, C. G. Péterfalvi, G. Burkard, and J. R. Petta, High-Resolution Valley Spectroscopy of Si Quantum Dots, *Phys. Rev. Lett.* **119**, 176803 (2017).
- [23] M. Friesen and S. N. Coppersmith, Theory of valley-orbit coupling in a Si/SiGe quantum dot, *Phys. Rev. B* **81**, 115324 (2010).
- [24] A. Hollmann, T. Struck, V. Langrock, A. Schmidbauer, F. Schauer, T. Leonhardt, K. Sawano, H. Riemann, N. V. Abrosimov, D. Bougeard, et al., Large, Tunable Valley Splitting and Single-Spin Relaxation Mechanisms in a Si/Si_xGe_{1-x} Quantum Dot, *Phys. Rev. Applied* **13**, 034068 (2020).
- [25] D. M. Zajac, T. M. Hazard, X. Mi, K. Wang, and J. R. Petta, A reconfigurable gate architecture for Si/SiGe quantum dots, *Appl. Phys. Lett.* **106**, 223507 (2015).
- [26] J. R. Petta, J. M. Taylor, A. C. Johnson, A. Yacoby, M. D. Lukin, C. M. Marcus, M. P. Hanson, and A. C. Gossard, Dynamic Nuclear Polarization with Single Electron Spins, *Phys. Rev. Lett.* **100**, 067601 (2008).
- [27] See the Supplemental Material at [url will be inserted by publisher] for a description of the experimental setup, calibration method, parameters estimated, details of the theoretical model.
- [28] E. Kawakami, P. Scarlino, D. R. Ward, F. R. Braakman, D. E. Savage, M. G. Lagally, M. Friesen, S. N. Coppersmith, M. A. Eriksson, and L. M. K. Vandersypen, Electrical control of a long-lived spin qubit in a Si/SiGe quantum dot, *Nature Nanotechnology* **9**, 666 (2014).
- [29] R. Ferdous, E. Kawakami, P. Scarlino, M. P. Nowak, D. R. Ward, D. E. Savage, M. G. Lagally, S. N. Coppersmith, M. Friesen, M. A. Eriksson, et al., Valley dependent anisotropic spin splitting in silicon quantum dots, *npj Quantum Information* **4**, 26 (2018).
- [30] M. Veldhorst, R. Ruskov, C. H. Yang, J. C. C. Hwang, F. E. Hudson, M. E. Flatté, C. Tahan, K. M. Itoh, A. Morello, and A. S. Dzurak, Spin-orbit coupling and operation of multivalley spin qubits, *Phys. Rev. B* **92**, 201401 (2015).